energy&fuels

pubs.acs.org/EF

Article

Experimental and Numerical Analysis of the Effects of Clay Content on CH_4 Hydrate Formation in Sand

Alejandro Bello-Palacios,* Stian Almenningen, Per Fotland, and Geir Ersland

Cite This: *Energy Fuels* 2021, 35, 9836−9846

Read Online

ACCESS | Metrics & More | Article Recommendations

ABSTRACT: Natural gas hydrates exist in large quantities in nature and represent a potential source of energy, mostly in the form of methane gas. Knowledge about hydrate formation in clayey sand is of importance for understanding the production of methane gas from hydrate reservoirs, as well as for understanding the impact of global warming on the stability of subsurface gas hydrates. In this paper, we explore the effect of clay content on methane gas hydrate phase transitions in unconsolidated sand at realistic reservoir conditions (P = 83 bar and T = 5−8 °C) both experimentally and numerically. Kaolin clay was mixed in pure quartz sand in a series of experiments where the clay content ranged from 0 wt % to approximately 12 wt %. Simulations of these experiments were set up in TOUGH+HYDRATE. In the kinetic reaction model, particle size was used as a proxy for kaolin content. The growth of methane hydrates from water (0.1 wt % NaCl) and methane were visualized and quantified by magnetic resonance imaging with millimeter resolution. Dynamic imaging of the sand revealed faster hydrate growth in regions with increased clay content. NMR T_2 mapping was used to infer the hydrate phase transition characteristics at the pore scale. Numerical simulations showed also faster growth in materials with a smaller mean particle size. The simulation results showed a significant deviation throughout the hydrate growth period. The constraints of both the experimental and modeling setups are discussed to address the challenges of comparing them.

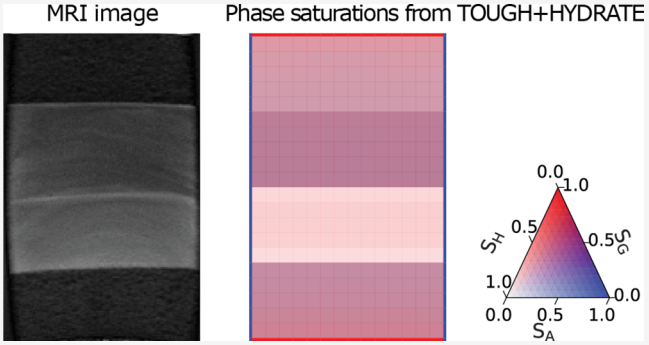

INTRODUCTION

Background. The amount of methane gas associated with natural gas hydrates in nature has led to a proliferation of research on gas hydrates in porous media. Several countries have state-sponsored research programs aimed at quantifying the domestic resource potential and enabling safe methane gas production from hydrate reservoirs. The trial productions that have been undertaken over the past two decades highlight the difficulty of maintaining sustained gas production by field-scale hydrate dissociation.[1−3] The preferred production method is to dissociate the hydrate structure into water and methane by pressure depletion and let the pressure differential between the dissociation front and the wellbore drive the production of fluids.[4] The hydrate accumulations most likely for gas production are located in the pore space of sandy sediments.[5] The presence of solid hydrates in the pore space enhances the effective cohesion of the sediments and has a stabilizing effect on the integrity of the formation.[6] The combined effect of pressure depletion and conversion of solid hydrates to fluids can trigger mobilization of sediments and collapse of the formation.[7,8] A review of all field pilots conducted to date shows that all tests have to some extent experienced problems with uncontrolled sand production.[9] The sandy sediments that are usually targeted as promising hydrate accumulations also contain varying amounts of clay particles that may be mobilized during hydrate dissociation. The transportation of small particles, i.e., fines, may alter the permeability of the formation by either enhancing it in the pores where the fines are displaced or decreasing it in the pores where the fines are deposited.[10] In either way, the impact of clay particles should be addressed in laboratory experiments to mimic the flow behavior of water and gas in unconsolidated sediments.

Clay Content in Hydrate Bearing Sediments. The impact of clay particles on hydrate phase stability is important when assessing the potential of finding large accumulations of hydrates in different lithologies. High hydrate accumulations are typically found in coarse-grained sand where the connectivity of the pore bodies is good, leading to an even distribution of methane throughout the pore space. Increased clay content is associated with narrower pores that limit the

Received: February 18, 2021
Revised: May 7, 2021
Published: May 31, 2021

accumulation of hydrates but can locally cause volumes of high saturation, i.e., almost pure hydrate. These pure hydrate volumes are however not connected as in coarse-grained sand, but rather display a veined and patchy distribution. Waite et al.[11] explored the correlation between hydrate saturation and clay content in sandy sediments from the Krishna-Godavari Basin, the Cascadia Margin,[12] and the Nankai Trough.[13] The clay content was defined as the volume fraction of grains smaller than 4 μm. The hydrate saturation was close to zero in sediments with clay fractions larger than 0.3, while elevated hydrate saturations larger than 0.4 and 0.6 were found in sediments with clay fractions less than 0.1 and 0.05, respectively. The clay content thus seems to effectively control the saturation of hydrates found in nature. However, the effect on hydrate phase equilibria depends on the specific clay mineral. Kaolin clay with water content less than 20 vol % yielded methane hydrate equilibrium temperatures that were up to 1.5 °C lower than bulk hydrate.[14] A similar hydrate inhibition was observed for glass beads with a particle size slightly higher than that of kaolin clay. The inhibition effect of kaolin clay was thus explained as a pore size phenomenon. The equilibrium temperature was also depressed in bentonite clay, except when the water content was larger than approximately 90 vol %. Then, the equilibrium temperature was slightly elevated and hydrate formation was promoted. In another study, the presence of bentonite clay in a suspension of silica sand and seawater decreased the induction time of hydrate formation and enhanced the rate of gas consumption compared to silica sand alone.[15]

Numerical Simulation of Gas Hydrates in Porous Media. Hydrate reservoir simulators are essential to forecast the long-term production performance of hydrate-bearing reservoirs.[16] Multiple tools have been tested and compared[16,17] to validate and build confidence in the modeling of hydrate-related processes in porous media.

In general, these tools involve coupling of physical, chemical, and thermal processes.[16] Formation and dissociation of hydrates are commonly modeled as either an equilibrium phenomenon or a kinetic reaction.[18] In the first approach, two main components (water and gas) can be found present in different phases, depending on the conditions of pressure and temperature. In the second approach, hydrate is treated as a new mass component and phase transitions are calculated from the kinetic parameters of the model. Multiple models developed to represent kinetic hydrate formation have been proposed. Yin et al.[19] has mapped out a total of 27 well-known hydrate growth kinetic models. Just a few models have been developed and implemented in reservoir simulation codes to model hydrate growth in porous media.[20−23] All these models are defined by an Arrhenius-type reaction rate constant. Another factor that steers the gas consumption is the surface area, which can be defined by time-dependent[22] or hydrate-saturation-dependent[20,21,23] factors. In addition, a driving force is defined by the difference in the fugacity of methane between the gas phase and the three-phase equilibrium[20,21,23] or the difference in chemical potential between water in the hydrate and liquid phases.[22]

The TOUGH+HYDRATE v1.5 (T+H)[24] code and its open-source version HydrateResSim[25] are codes developed by Lawrence Berkeley National Laboratory. Both codes have been used in the numerical evaluation of natural occurrences of gas hydrates[26−29] and to model experiments on hydrate formation.[30,31] The code has been developed to simulate the behavior of methane hydrate bearing sediments and handles both multiphase, multicomponent flow and transport of mass and heat through porous and fractured media.[21]

In T+H hydrate formation and dissociation are modeled by using either a kinetic or equilibrium model. Kowalsky and Moridis[32] have concluded that the kinetic model is more suitable for modeling short-term and core-scale processes.

The kinetic model in T+H is defined by eq 1.[33]

$$\frac{\partial M}{\partial t} = K_0 e^{(-\Delta E_a/RT)} F_A A_S (f_{eq} - f_v) \quad (1)$$

where $\frac{\partial M}{\partial t}$ is the methane mass rate of change, K_0 is the intrinsic hydration reaction constant, ΔE_a is the hydration activation energy, R is the universal gas constant, T is the temperature, F_A is the area adjustment factor, A_S is the hydrate reactive surface area, f_{eq} is the fugacity at equilibrium temperature, and f_v is the fugacity in the gas phase at temperature T.

Equation 1 yields the uptake of gas for hydrate formation in time (Figure 1). Changes in the gas consumption rate follow

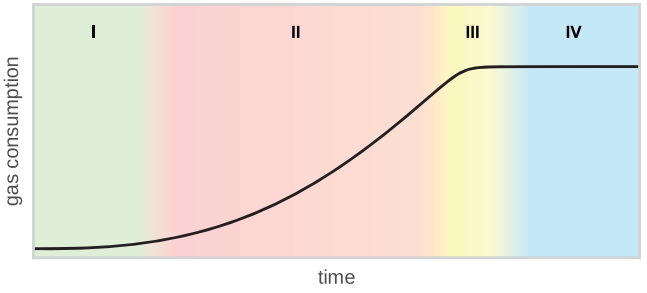

Figure 1. T+H modeled gas uptake curve during gas hydrate formation from the kinetic model. Colors highlight the different stages in hydrate formation described by Yin et al.[19] Induction time (stage I), rapid hydrate growth (stage II), decreased growth (stage III), and steady state (stage IV).

the typical gas uptake curve described by Yin et al.[19] in four stages. The early slow growth mimics an induction time (stage I), followed by a steep growth where most of the gas intake occurs (stage II) until it slows down (stage III) and reaches a steady state (stage IV).

There are no specific parameters in the model that respond to the presence of clay. However, the size of particles, the porosity of the sediment, and the hydrate saturation are the input parameters that define the reactive surface area (A_S), which has an impact on the hydrate growth and dissociation rates. The magnitude of A_S is a function of the average grain radius of the sediment r_p, its porosity ϕ, and the hydrate saturation S_H at a given time (eq 2[33]).

$$A_S = 0.879 \frac{1-\phi}{r_p} S_H^{2/3} \quad (2)$$

In this study, we examine the effect on methane hydrate phase transitions by adding kaolin clay to quartz sand. Specifically, we map the saturation of methane hydrates during formation at reservoir conditions by magnetic resonance imaging (MRI). The weight percent of kaolin clay compared to quartz sand was low (lower than 13 wt %) to emphasize the effect of the surface texture of kaolin clay on hydrate phase transitions.

T+H was used to reproduce numerically the experimental observations. To validate the kinetic reaction model, particle

https://doi.org/10.1021/acs.energyfuels.1c00549
Energy Fuels 2021, 35, 9836−9846

size is used as a proxy of clay content. We study how variations in particle size affect the modeled hydrate growth. Model outputs are compared with experimental measurements to identify the strengths and limitations of the code.

The results of this work are relevant for both experimental analysis and numerical analysis of hydrate accumulations in coarse-grained sand reservoirs containing clay.

METHODS

Experimental Setup. Quartz sand (D50 = 220 μm) mixed with kaolin clay (D50 = 3.5 μm) was used as host sediment for the methane hydrate phase transitions in this study. Dry kaolin clay was added to the sand and mixed thoroughly by rotating a beaker. The rubber sleeve was placed vertically with a fluid-distributing end piece inserted at the bottom. Different mixtures of sand and clay were then placed in sections inside the rubber sleeve on top of each other. Consolidated Bentheim sandstone core pieces were placed as filters at both ends between the body of sand and the end pieces to avoid sand production. The average pore diameter of Bentheim sandstone is 125 μm.[34] The core holder, high-pressure pumps, cooling system, and superconductive magnet used for MR imaging are detailed in Almenningen et al.[35]

Experimental Procedure. Two different experimental runs were conducted with two different designs. In the first experiment (experiment 1, Figure 2), the length of the rubber sleeve was filled with Bentheim sandstone (L = 2.42 cm), pure quartz sand (L = 2.30 cm), quartz sand containing 0.9 wt % kaolin clay (L = 2.80 cm), and Bentheim sandstone (L = 2.13 cm). In the second experiment (experiment 2, Figure 1), the length of the rubber sleeve was filled with Bentheim sandstone (L = 2.15 cm), quartz sand containing 3.4 wt % kaolin clay (L = 2.00 cm), quartz sand containing 6.1 wt % kaolin clay (L = 2.15 cm), quartz sand containing 12.4 wt % kaolin clay (L = 2.20 cm), and Bentheim sandstone (L = 2.12 cm). A core holder was mounted around the rubber sleeve, and an effective confining pressure of 15 bar was applied before the core holder was placed horizontally.

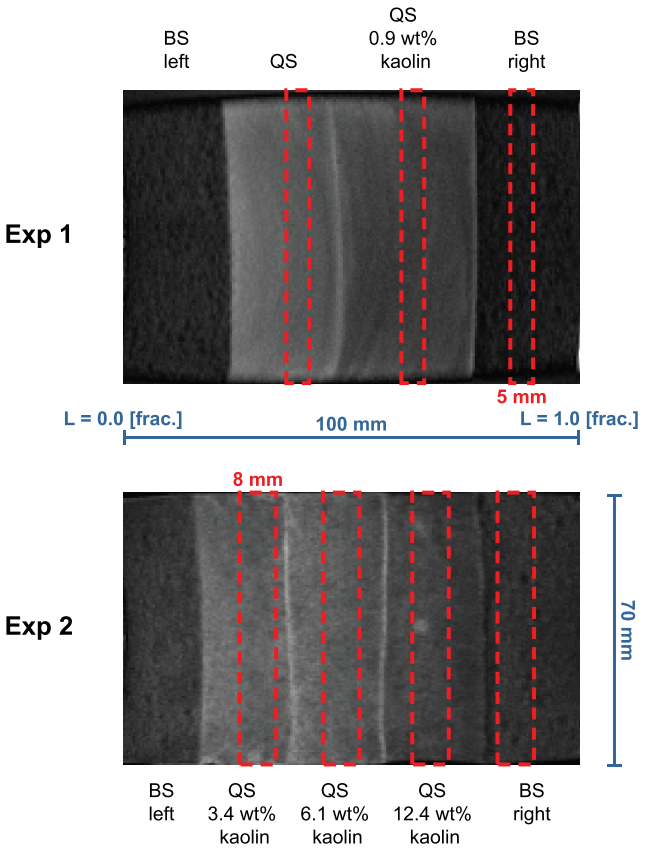

Figure 2. Sagittal view of quartz sand (QS) and Bentheim sandstone (BS) saturated with brine inside the core holder. The red dashed rectangles mark the positions of the axial MRI slices that were used to analyze hydrate formation (5 mm thick for experiment 1 and 8 mm thick for experiment 2).

The pore space was purged under vacuum and subsequently saturated with brine containing 0.1 wt % NaCl. Injection of methane gas from one side of the core material displaced some of the brine, and the pore space was consequently filled with a mixture of methane gas and brine. In experiment 1, to achieve a continuous phase of gas along the core setup, methane gas was injected until there was a gas breakthrough at the other end. In experiment 2, the gas inflow was stopped prior to gas reaching the other end, so the right section of the core setup would be 100% saturated with brine.

Hydrate formation was then triggered by cooling the system to 7 °C and increasing the pore pressure to 83 bar by methane gas injection from both sides of the core material. The 2-D saturation maps of brine and methane hydrates were continuously acquired during hydrate growth. Bulk hydrate saturation (S_h) was calculated from the amount of methane consumed by the system, using *PVT* data. Simultaneously, an explicit mapping of hydrate saturation (S_h) was obtained by tracking the changes in water saturation observed in the MRI images, assuming that all reduction in water saturation was caused by hydrate formation. This assumption is reasonable for hydrate growth at constant pressure.[35]

Modeling Setup. The physical system was represented in both a one-dimensional grid and a two-dimensional grid. The different contents of kaolin were interpreted as a variation of particle size.

The magnitude of the area adjustment factor (F_A) value was reduced iteratively until the time scales of both the experiments and simulations were of the same order of magnitude. F_A can be adjusted to match observations in history matching simulations.[21] Yin et al.[31] has determined that F_A may not remain constant during hydrate formation. In our study, the magnitude was kept constant through the whole simulation.

One-Dimensional Model. A one-dimensional grid was built to have bulk estimates of the growth of hydrates through time and final phase saturations. This model assumes both brine and gas are evenly distributed and in contact with each other. The system was initialized by having brine and gas at 7 °C. The pressure is calculated by T+H to near 53 bar, just next to the boundary of stability for the given salinity (0.3 wt % NaCl). As soon as hydrates start forming, the pressure and temperature are sustained by a thermodynamic boundary. This boundary is set to keep the pressure and temperature at 83 bar and 7 °C, by injecting gas and steering the flow of heat.

This model was used first to calculate the final hydrate saturation of experiments 1 and 2, based on their initial fluid phase saturations. Then, the model was used to study the effect of initial fluid saturation and particle size on hydrate growth driven by the kinetic reaction model of T+H. These simulations were set by initializing the model with a broad range of brine saturation (S_{wi}) and particle sizes (r_p), ranging from 50 to 110 μm.

Two-Dimensional Model. Two-dimensional grids were built representing both experiments (Figure 3). The grid represents a sagittal horizontal slice of the core, discretized by 280 cubic elements (20 × 14) of 50 mm on edge length. The grid is surrounded by infinite boundaries that steer both mass and heat flow. Along the longest axis, the boundary is impermeable and is set to deliver the necessary heat flow to keep the system at the target temperature. The boundaries along the shortest axis represent the core end pieces and behave like those in the 1-D model.

The grid was split into regions emulating the different core pieces for each core setup (Figure 3). No measurements of porosity, permeability, and other thermophysical properties were available for the sand mixtures used. Therefore, all intrinsic thermophysical properties other than the particle size were assumed equal for all regions (Table 1).

https://doi.org/10.1021/acs.energyfuels.1c00549
Energy Fuels 2021, 35, 9836−9846

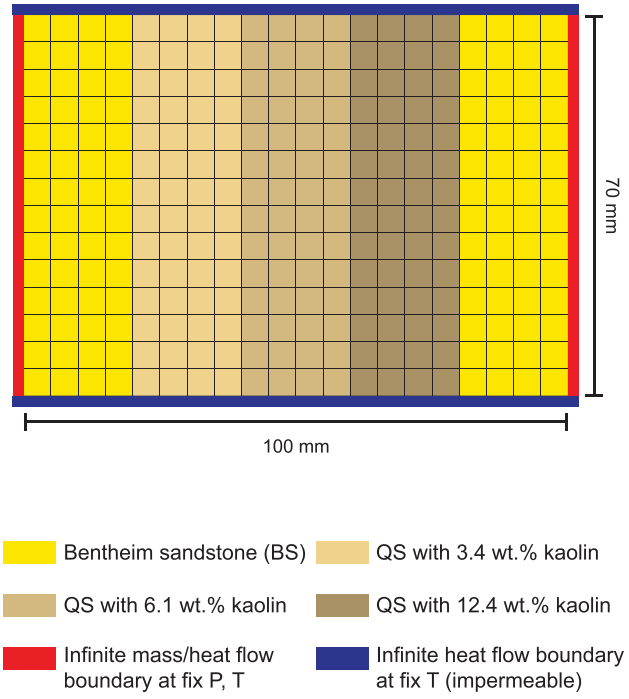

Figure 3. Two-dimensional simulation grid for experiment 2. The infinite boundary in red is set to deliver the necessary mass and heat flow to keep the system at the target pressure and temperature. The infinite boundary in dark blue is impermeable and is set to deliver the necessary heat flow to keep the system at the target temperature.

The particle size (r_p) was adjusted with the grain size of the clean quartz sand used in the experiments as reference (110 μm). The remaining sand mixtures were adjusted under the premise that sand with a larger amount of kaolin would have a smaller representative mean grain radius. The particle size of Bentheim sandstone was also adjusted to match results.

Unlike the 1-D models, simultaneous hydrate growth at different rates occurs in different locations of the model. To focus only on the effects of particle size and to keep the model numerically stable, the intrinsic permeability was set to remain unaffected by the presence of a solid hydrate phase. Other thermophysical properties were left unchanged for all grid cells, with their magnitudes based on Bentheim sandstone values used by Birkedal et al.[36] Simulations were run with the capillary pressure function both enabled and disabled. With the latter setup, the fluid flow would be driven only by pressure differences in the system (Darcy flow). The multiphase flow would be therefore governed solely by relative permeability curves (Table 1).

RESULTS

Experimental Results. Prior to hydrate formation, the initial average water saturation was 0.62 (fraction) with a near even distribution throughout the core (Figure 4). As hydrate started forming, the liquid water saturation decreased faster in the quartz sand containing 0.9 wt % kaolin compared to the rest of the sediments. This means that the initial hydrate growth was significantly faster in quartz sand containing 0.9 wt % kaolin than in Bentheim sandstone and pure quartz sand (Figure 10a). However, a residual liquid water saturation remained at approximately 0.06 fraction after hydrate formation ceased at an average hydrate saturation of 0.71 (fraction). After hydrate formation, the apparent gas permeability was zero, indicating complete blocking of the pore space.

The initial water distribution was heterogeneous in experiment 2 (Figure 5) with an increasing water saturation from 0.50 (fraction) at $L > 0.75$ (fraction) to 1.0 (fraction) at $L <$ 0.30 (fraction). The average water saturation was 0.76

Table 1. Thermophysical Properties of Materials and Parameters Used in Simulation Model

parameter	value[a]
gas composition	100% CH_4
intrinsic hydration reaction constant (K_0)	4.70848×10^5 mol/(m^2·Pa·s)[37]
hydration activation energy (ΔE_a)	8.1×10^4 J/mol[37]
universal gas constant (R)	8.314 J/(mol·K)
intrinsic permeability ($k_x = k_y = k_z$)	1.5 D (1.48×10^{-12} m^2)
porosity (ϕ)	0.30 fraction
density (ρ)	2650 kg/m^3
thermal conductivity, dry (λ_d)	0.30 W/m/K
thermal conductivity, fully saturated (λ_w)	1.65 W/m/K
specific heat (c_p)	1400 J/kg/K
boundary thermal conductivity (λ_b)	0.20 W/m/K
boundary specific heat ($c_{p,b}$)	1000 J/kg/K
composite thermal conductivity model (λ)	$\lambda = \lambda_d + (S_W^{1/2} + S_H^{1/2})(\lambda_w - \lambda_d)$
modified relative permeability model[38]	$k_{rA} = \left(\frac{S_W - S_{irW}}{1 - S_{irW}}\right)^{n_W}$
	$k_{rG} = \left(\frac{S_G - S_{irG}}{1 - S_{irW}}\right)^{n_G}$
	$k_{rH} = 0$
	$n_W = n_G = 3.0$
	$S_{irW} = 0.12$, $S_{irG} = 0.02$
capillary pressure model[39]	$P_{cap} = -P_0[(S^*)^{-1/\lambda} - 1]^{1-\lambda}$
	$S^* = \frac{S_W - S_{irW}}{S_{mxA} - S_{irW}}$
	$\lambda = 0.6$, $S_{irW} = 0.11$
	$P_0 = 2 \times 10^3$, $S_{mxA} = 1.0$

[a]Subscripts "W", "G", and "H" represent aqueous, gas, and hydrate phases, respectively; S_X is the phase saturation; S_{irX} is the irreducible phase saturation.

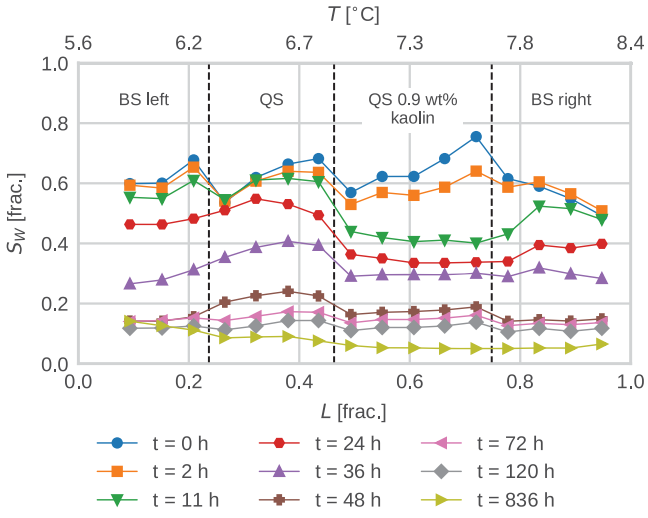

Figure 4. Change in water saturation during hydrate growth at constant pressure, P = 83 bar, in experiment 1.

https://doi.org/10.1021/acs.energyfuels.1c00549
Energy Fuels 2021, 35, 9836−9846

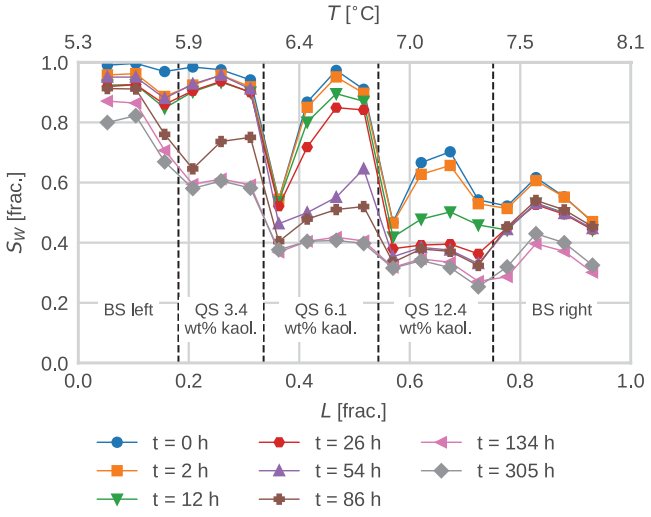

Figure 5. Change in water saturation during hydrate growth at constant pressure, P = 83 bar, in experiment 2.

(fraction) prior to hydrate formation. As hydrate started forming, the liquid water saturation decreased faster in the quartz sand containing 12.4 wt % kaolin compared to other parts of the sediment. This means that the initial hydrate growth was faster in quartz sand containing the most kaolin during the first 26 h of hydrate formation (Figure 11a). Next, from t = 26 h to t = 54 h, a massive hydrate growth occurred in the quartz sand containing 6.1 wt % kaolin. The growth of hydrate was limited in the rest of the sediments during this period. Massive hydrate growth followed in the quartz sand containing 3.4 wt % kaolin from t = 54 h to t = 86 h. The growth of hydrate was thus sequential, moving from quartz sand with high kaolin content to quartz sand with low kaolin content. The final water and hydrate saturation after hydrate formation were 0.51 and 0.33 (fraction), respectively.

The transverse relaxation time constant T_2, which increases with pore size, showed a different response as the content of clay increased (Figure 6). In quartz sand with 3.4 wt % kaolin, the intermediate to large T_2 (pore size) components disappeared during hydrate growth. However, in quartz sand containing 12.4 wt % kaolin, it was the intermediate to low T_2 components that disappeared during hydrate growth.

Modeling Results. *One-Dimensional Model.* The first set of results from the 1-D simulations is shown in Figures 7 and 8. In the one-dimensional simulation for experiment 1, the final hydrate saturation after hydrate formation was 0.74 (fraction). The remaining volume is filled by mainly gas (0.25) and a small fraction of brine (less than 0.01). For experiment 2, the final hydrate saturation after hydrate formation was 0.91 (fraction). The remaining volume is filled by mainly gas (0.08) and a small fraction of brine (less than 0.01). Given the assumptions of the model, the system consumes all the water to form hydrates. The remaining water saturation is a result of inhibition due to increased salinity (8.7 wt % NaCl).

The second set of results from the 1-D simulations is shown in Figure 9. Each simulation produced a hydrate growth (gas uptake) curve in time, defined by the kinetic model and variations on the input parameters. Decrease of particle size resulted in a shorter induction time (stage I) and a higher rate during the main hydrate growth (stage II). Initial brine saturation (S_{wi}) has a direct impact on the magnitude of

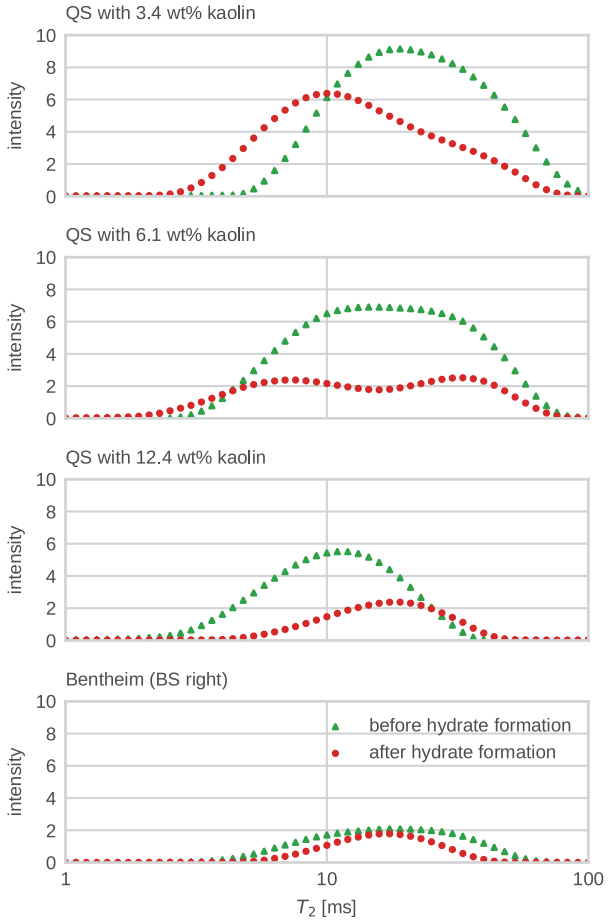

Figure 6. T_2 distributions before and after hydrate growth in experiment 2.

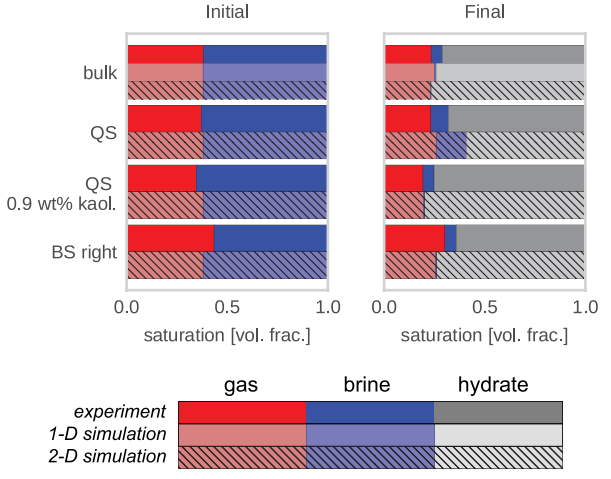

Figure 7. Experiment 1. Comparison of average phase saturations yielded by experiments and simulations for the entire core setup (bulk) and each core piece. Initial values prior to hydrate formation on left and final post hydrate formation values on right. Experimental measurements in bold colors, 1-D simulation results in lighter colors, and 2-D simulation results in dashed colors.

hydrate saturation at which hydrate growth slows down and reaches a steady state (stages III and IV).

Two-Dimensional Model. Results for 2-D simulations of experiments 1 and 2 are included in Figures 10b and 11b,

https://doi.org/10.1021/acs.energyfuels.1c00549
Energy Fuels 2021, 35, 9836−9846

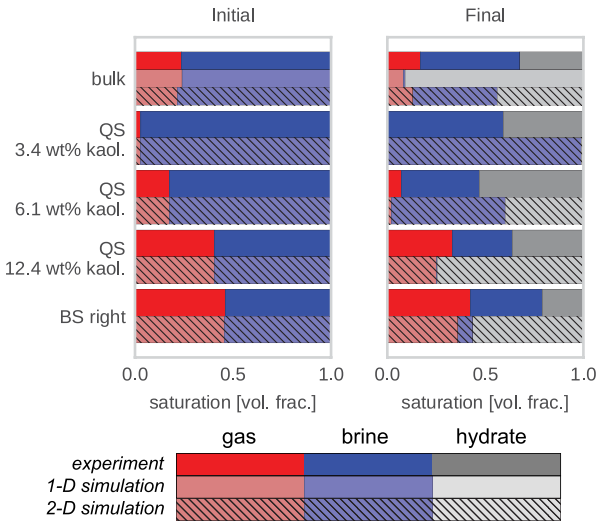

Figure 8. Experiment 2. Comparison of average phase saturations yielded by experiments and simulations for the entire core setup (bulk) and each core piece. Initial values prior to hydrate formation on left and final post hydrate formation values on right. Experimental measurements in bold colors, 1-D simulation results in lighter colors, and 2-D simulation results in dashed colors.

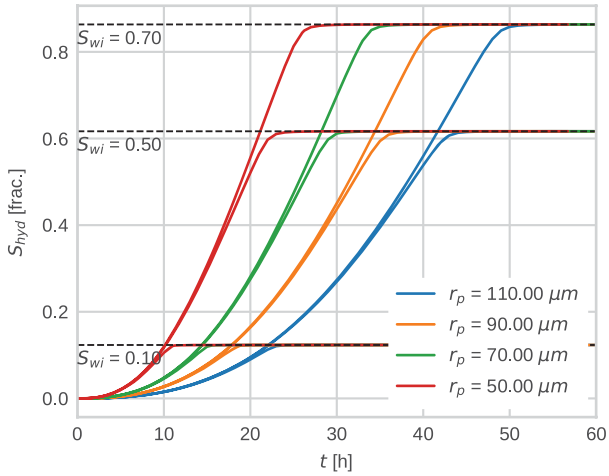

Figure 9. Effect of mean particle radius (r_p) and initial brine saturation (S_{wi}) on hydrate growth. Each simulation result shows hydrate saturation change through time for different cases, initialized with a specific particle size (50−110 μm) and initial brine saturation (0.1−0.7 fraction).

respectively for comparison with experimental measurements. In addition, extended visualizations in time for both experiments are included in Figures 12 and 13.

For experiment 1, small variations in the distribution of phases were neglected and simulations were initialized by having a homogeneous two-phase distribution of gas (0.38 fraction) and brine (0.62 fraction). Enabling the capillary function did not result in major changes in the simulations; therefore, the results presented in this section concern only the simulations run without the capillary function enabled. The area adjustment factor (F_A) was reduced to 1.59×10^{-3} to stretch the reaction time and match the experimental data. Mean particle sizes of the media representing Bentheim

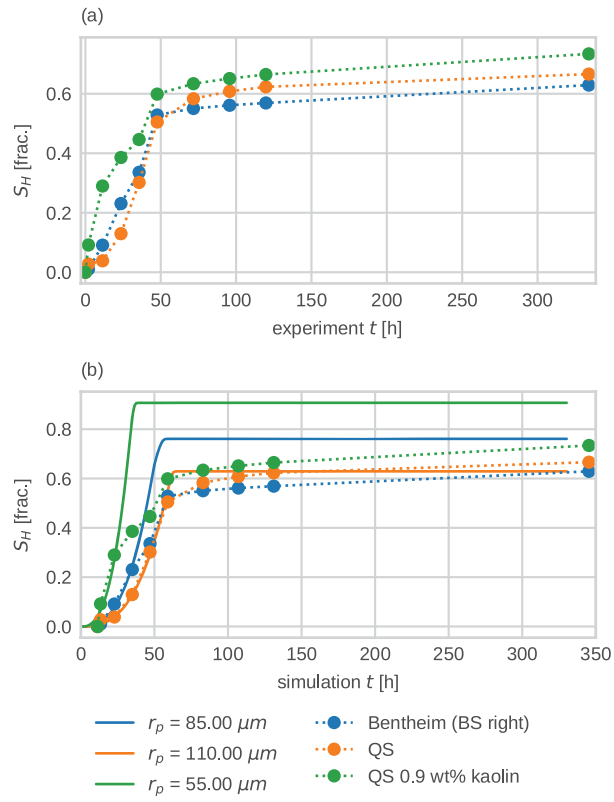

Figure 10. Experiment 1. (a) Time development of hydrate saturation in quartz sand (QS), quartz sand containing 0.9 wt % kaolin, and Bentheim sandstone (BS right). (b) In continuous lines, simulated hydrate saturation for the corresponding sections. Area adjustment factor (F_A) set to 1.59×10^{-3}. Experimental measurements are added for comparison with a time shift to compensate nondetectable slow growth within the first hours of simulation.

sandstone and quartz sand containing 0.9 wt % kaolin were adjusted to 85 and 55 μm, respectively. The simulation time for experiment 1 was shifted to compensate for the early slow hydrate growth that can be undetected experimentally. Such a shift accounted for the first 10 h of simulation (Figure 10b). Initial hydrate growth was faster in the material with the smallest particle size (55 μm) and leveled out around 0.91 (fraction). Hydrate growth continued at a slower rate as the particle size increased. The final hydrate saturation leveled off in 85 and 110 μm at 0.76 and 0.63 (fraction), respectively. The final bulk water and hydrate saturation after hydrate formation were 0.01 and 0.76 (fraction) (Figures 10b and 12).

Experiment 2 was initialized with a heterogeneous distribution of fluids along the core. Enabling the capillary function prevented the simulation from preserving the heterogeneous distribution of fluids. Therefore, this feature was disabled and the results presented for the simulations of experiment 2 do not consider capillary pressure. To keep consistency with experiment 1, the particle size of Bentheim sandstone was set to 85 μm and the particle sizes of the sand mixtures containing 3.4, 6.1, and 12.4 wt % kaolin were set to 50, 45, and 40 μm, respectively. Hydrate growth responds to both the particle size and the mobility of gas throughout the system. Although hydrate growth starts earlier in the quartz sand containing 3.4 wt % kaolin (50 μm), hydrate growth in the Bentheim sandstone (85 μm) rapidly stagnates around

https://doi.org/10.1021/acs.energyfuels.1c00549
Energy Fuels 2021, 35, 9836−9846

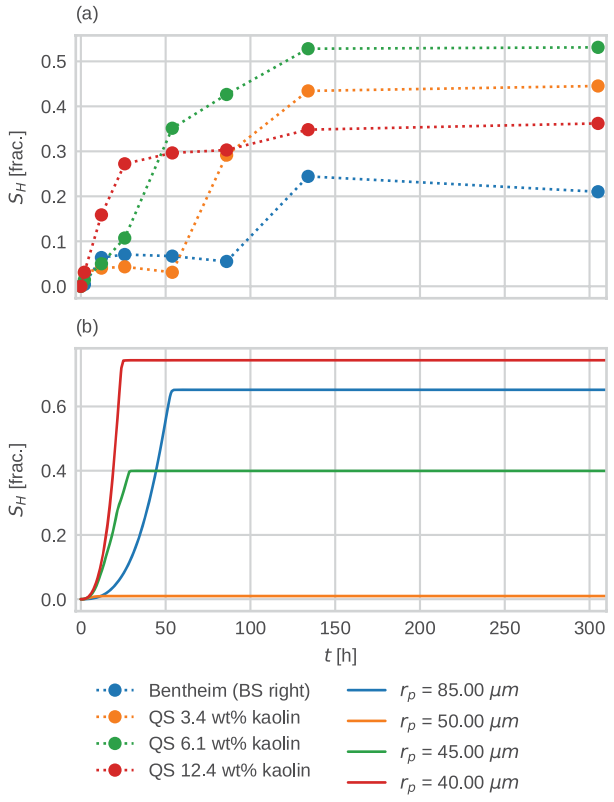

Figure 11. Experiment 2. (a) Time development of hydrate saturation in quartz sand (QS) containing 3.4, 6.1, and 12.4 wt % kaolin, and Bentheim sandstone (BS right). (b) Simulated hydrate saturation for the corresponding sections. Area adjustment factor (F_A) set to 1.59 × 10^{-3}.

0.01 (fraction). A similar process is observed in the quartz sand containing 6.1 wt % kaolin (45 μm). The modeled sequential hydrate growth was found to be very sensitive to variability in the initial distribution of fluids and the dynamics governing the boundary conditions. The final bulk water and hydrate saturation after hydrate formation were 0.43 and 0.44 (fraction), respectively (Figures 11b and 13).

Exchange of brine and gas between each grid section was tracked for both 2-D simulations. Most of the water that took part in hydrate formation at each core piece was observed to be sourced mainly from the initial water saturation of that grid region. Very small amounts of brine were exchanged between them. Active fluxes of gas between each grid region occurred and were only hindered by the regions with high saturation of brine in 2-D simulations for experiment 2 (Figure 13).

DISCUSSION

Effect of Clay on Hydrate Formation Rate. Results from both experiments reveal how the initial water distribution governs the final water and hydrate distribution. This is evident from Figures 4 and 5 and has also been verified earlier by Almenningen et al.[35]

The variation of initial water saturation along the length of the sediments in experiment 2 explains also part of the observed sequential growth rate of hydrate. However, it does not account for the slow and limited hydrate formation in the Bentheim sandstone at $L > 0.75$ (fraction); water saturation was in fact the lowest (0.54 volume fraction) and most ideal for hydrate formation.

The sequential growth of hydrate is also contrary to the applied temperature gradient; the temperature was decreasing from right to left (8.1 °C at $L = 1$ fraction, 5.3 °C at $L = 0$ fraction). The observed sequential growth rate of hydrate may therefore be explained by the content of kaolin in the quartz sand. Small kaolin particles fill the pore space between the quartz sand particles, and the observed growth rate of hydrate may be a pore size phenomenon.[40] The surface energy and texture of kaolin particles may also affect the nucleation of hydrate. This may be explained by a shift in the pore-scale

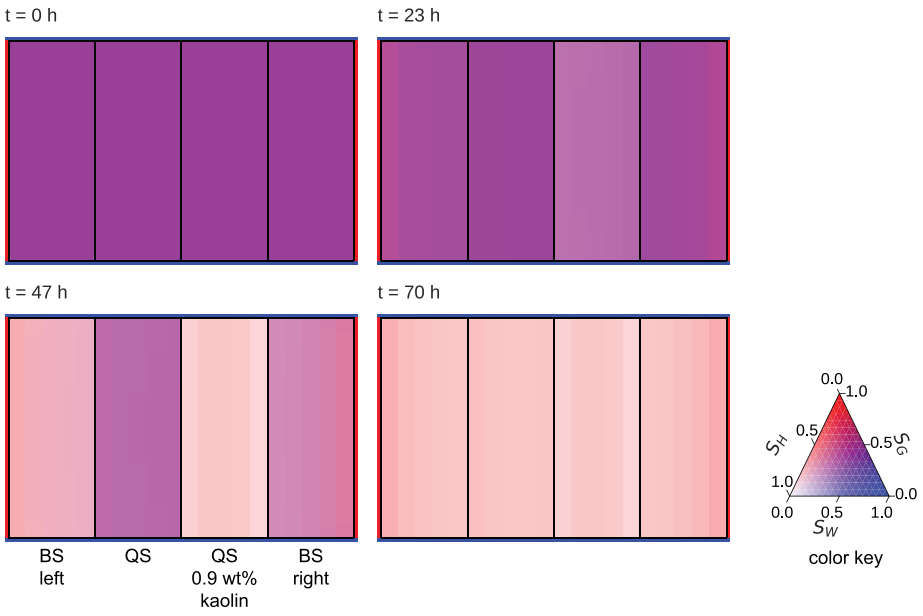

Figure 12. Experiment 1. Visualization of 2-D simulation results at different points in time. The color shade is proportional to the saturation of each phase. Hydrate (white), brine (blue), and gas (red). The last visualization is shown when hydrate growth has reached a steady state.

https://doi.org/10.1021/acs.energyfuels.1c00549
Energy Fuels 2021, 35, 9836−9846

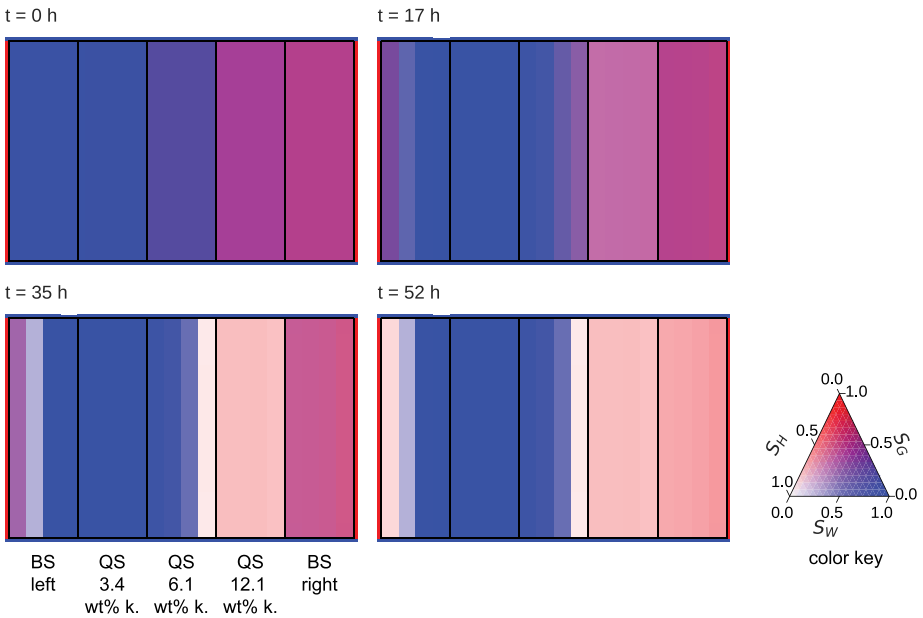

Figure 13. Experiment 2. Visualization of 2-D simulation results at different points in time. The color shade is proportional to the saturation of each phase. Hydrate (white), brine (blue), and gas (red). The last visualization is taken within the time all hydrate growth has reached a steady state.

hydrate growth pattern when the kaolin content exceeds a threshold.

The shift in average T_2 suggests a change in the pore-scale hydrate growth pattern when the kaolin content is changing. The loss of short T_2 components in quartz sand with high kaolin content implies hydrate formation close to the surface of clay and quartz particles.

Comparison between Numerical and Experimental Results. Simulation results show major deviations from the experimental results. The simulated systems are constrained by the assumptions in the model, and some mechanisms in the hydrate growth may not be accounted for.

It is, however, possible to make a qualitative comparison and attempt to understand where the limitations of the simulation model are. These limitations are analyzed from the methods used by T+H to model both hydrate growth and multiphase flow in the presence of hydrates, and how these affect each other. Both modeled hydrate growth and measured hydrate growth (Figures 9−11) are described in terms of the different stages of growth, based on the work by Yin et al.[19]

Induction Time (Stage I). Kowalsky and Moridis[32] have pointed out that the kinetic model does not account for nucleation phenomena. In the coarse grid used in this study, this results in the evolution of a homogeneous hydrate phase in each grid cell where formation is occurring. This effect makes the model deviate from the potential heterogeneous spatial distribution of hydrates.[40−42] However, the hydrate saturation reached toward the end of this stage is comparable to the early measurements made in both experiments (Figures 10 and 11).

Main Hydrate Growth (Stage II). Using particle size as a proxy for kaolin content provides a good approximation to model hydrate growth comparable to the experiments within the early part of this stage. Both experiments and simulations returned a sequential growth that was steeper in the core pieces with the highest content of kaolin (the smallest particle size) than in the pieces with little to no kaolin content.

Both experiments show changes in the hydrate growth rate at each core piece that may not be caused solely by the variations in the content of kaolin. The simulation results deviated largely from both experiments at this stage and did not manage to reproduce the observed changes in the hydrate growth rate. However, when different materials with different particle sizes are set adjacent to each other, the simulations show that hydrate growth is not constrained only by the kinetic model. When hydrate growth is modeled in homogeneous materials, the resulting hydrate growth is only a function of the particle size and the initial saturation of brine and gas. The particle size has a direct influence on how the growth reaches stages I and II of hydrate formation as seen in Figure 9. The initial fluid saturation determines at which point the growth will slow down and reach a steady state (stages III and IV). In the heterogeneous configuration of the 2-D grid (Figure 3), a new constraint is added to the modeled growth. Local formation of hydrates may have an impact on subsequent hydrate growth occurring in adjacent regions. These types of interferences are observed in 2-D simulations of both experiments. In the simulations of experiment 1, by the time growth in the Bentheim sandstone starts, hydrate formation in the quartz sand containing 0.9 wt % kaolin has already consumed part of the initial volume of brine. A similar situation is observed when hydrates are formed in the clean quartz sand. This effect results in each section of the grid reaching a progressively lower final saturation of hydrates (Figure 10b). In the simulations of experiment 2, the interaction between grid regions is more pronounced. The growth of hydrates is constrained not only by previous growth in other regions of the grid but also by the heterogeneous distribution of brine (Figure 11b). The high saturation of brine on the left side of the grid reduces the mobility of gas in this area. Although hydrate growth starts earlier in the sand with 3.4 wt % kaolin than in the Bentheim region, the growth slows down early and stagnates at a very low saturation (Figures 11 and 13). In the remaining materials, the growth rate at which

https://doi.org/10.1021/acs.energyfuels.1c00549
Energy Fuels 2021, 35, 9836−9846

each material reaches stage II varies according to their particle size. However, the final saturation at which growth slows down and reaches stage III is influenced mainly by the initial saturation of brine.

The different growth rates observed in both experiments may respond to interferences similar to those observed in the 2-D simulations. However, the lack of data characterizing the pore network properties of the materials and potential mechanisms not considered by T+H makes the modeling of such processes difficult.

The changes in flow patterns driven by local hydrate growth observed in the 2-D simulations are expected to behave differently if the effects of kaolin content and hydrate formation on pore network properties are considered. The different contents of kaolin in the sand mixtures are expected to have an impact on the intrinsic permeability and the relationships describing both the capillary pressure and relative permeability. The evolution of a solid hydrate phase is also expected to modify such properties. Although some of these mechanisms can be represented by T+H, they still need input data to narrow the range of uncertainty of the results.

Simulations of experiment 1 with and without capillary pressure function yielded near identical results and suggest that the displacements of methane and brine linked to the formation of hydrates are driven mainly by Darcy flow. However, in experiment 2, the capillary pressure function had immediate effects on the initialization of the system. When the capillary function model is enabled, the capillary pressure of each fluid phase is calculated. The fluid pressure of the nonwetting phase (methane) is assigned to 83 bar. The pressure in the wetting phase (brine) is close to 83 bar in the sections of the core where the brine saturation is close to 1.0 fraction, but it becomes less in the parts with lower brine saturation (Figure 14). This pressure gradient causes an almost

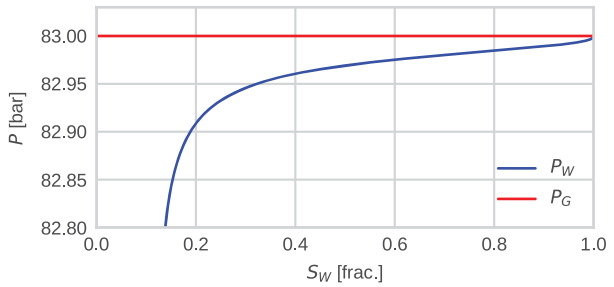

Figure 14. Fluid phase pressures of both water (P_W) and gas (P_G) when capillary pressure function is activated at varying water saturation (S_W). The system is confined 83 bar and uses model described in Table 1.

immediate redistribution of the fluid phases until there is no pressure imbalance. This mechanism hindered the use of the capillary pressure model and the analysis of the combined effects of kaolin and hydrate formation as well as the final saturation of hydrates.

The decrease in hydrate growth rate observed in the experiments can also be related to self-inhibitory hydrate formation mechanisms in porous media that cannot be represented by T+H. Hydrates have been observed to form randomly in pore spaces, causing local increases in saturation. These saturations can cause local hindrances for fluid flow,[43] which result in pores and throats becoming disconnected from each other and creating dead ends for flow.[44] Hydrate formation can also result in the evolution of both nonporous crystalline hydrates and porous hydrate shells with encapsulated fluids[45] that will no longer take part in the reaction within the time scale of the experiments.

Decrease in Growth and Steady State (Stages III and IV). Regarding the total amount of hydrate yielded, numerical simulations yielded contrasting results. Experiment 1 yielded almost as much hydrate as both 1-D and 2-D models did (Figure 7). At a core-piece level, both measurements and simulation show that the highest saturation of hydrate occurs in the quartz sand containing 0.9 wt % kaolin clay (Figure 7). The near homogeneous distribution of fluid phases prior to hydrate formation ensures an efficient contact between both fluid phases, resulting in a productive formation of hydrates in all core pieces.

One-dimensional simulations for experiment 2 showed a large deviation from both 2-D simulations and experimental measurements (Figure 8, right). The ideal system represented by the 1-D model guarantees that both gas and brine are always in contact, similar to experiment 1. With a heterogeneous distribution of brine, this is unlikely to happen. Two-dimensional simulations of experiment 2 yielded a bulk amount of hydrate comparable to that formed experimentally (Figure 8). The remaining brine saturation in the 2-D simulations (0.43 fraction) is also lower but comparable to the one yielded in the experiments (0.51 fraction).

In contrast, the heterogeneous water saturation in experiment 2 inhibits the system from forming hydrates as efficiently as 1-D simulations did. Both 2-D simulations and experimental results show that there is a large fraction of brine that does not react with gas (0.51 fraction) (Figure 8).

When each core piece is compared with its corresponding grid section in the 2-D model, the final distribution of hydrates shows large deviations (Figure 8). Most of the hydrate formation modeled in the 2-D simulations occurred in the right part of the system, in the regions representing the Bentheim sandstone (BS right) and the quartz sand containing 12.4 wt % kaolin (Figures 8 and 13). Limited to no growth is observed in the remaining grid regions. This is caused by the reduced mobility of gas. By the time hydrates start forming, the relative permeability is too low for methane to reach the inner parts of the system.

Thus, in terms of material balance, both 2-D models are able to form an amount of hydrate comparable to those acquired in the experiments. However, the limited characterization of the intrinsic properties of the system results in hydrates being distributed differently along the system. In addition, cross-flow of gas between layers causing changes of internal fluid saturations are observed. As mentioned above, hydrate growth may act as barriers for mass exchange and thus a significant amount of water may be disconnected from the gas phase and temporarily hinder hydrate formation. The detailed growth of hydrates that causes this combined effect will most likely be particular for a given experiment. However, for longer time scales and larger length scales, phenomena such as naturally occurring flow, diffusion, and Ostwald ripening are expected to drive the system toward an equilibrium situation within the local constraints of pressure and temperature gradients.

https://doi.org/10.1021/acs.energyfuels.1c00549
Energy Fuels 2021, 35, 9836−9846

CONCLUSIONS

- Methane gas hydrate phase transitions in unconsolidated quartz sand were imaged and the water distribution was mapped using MRI. The kaolin content of the sand ranged from 0 to 12 wt % in order to investigate the effect of clay on hydrate phase transitions.
- Experiments show that hydrate growth was significantly faster with increasing clay content. The final hydrate saturation was mainly governed by the initial water saturation.
- A shift in average T_2 during hydrate growth was observed for the highest clay content in sand. Hydrate was inferred to form close to the clay and sand surfaces when the sand contained 12 wt % clay, contrary to the pore-filling hydrate in sand containing less clay.
- One-dimensional models provided insight into the potential hydrate growth and final saturation in ideal conditions.
- By using particle size as a proxy for kaolin content, 2-D simulations reproduced a sequential hydrate growth similar to the one observed in the experiments.
- Deviations between simulations and experiments may be attributed to the effects of hydrates on intrinsic properties such as permeability and capillary pressure as well as the dynamic effects of local hydrate barriers and cross-flow between layers that is specific to each experiment.

AUTHOR INFORMATION

Corresponding Author

Alejandro Bello-Palacios − *Equinor ASA, 5020 Bergen, Norway; Department of Physics and Technology, University of Bergen, 5020 Bergen, Norway;* orcid.org/0000-0002-0294-9485; Phone: +47 941 56 014; Email: gpb@equinor.com

Authors

Stian Almenningen − *Department of Physics and Technology, University of Bergen, 5020 Bergen, Norway;* orcid.org/0000-0002-2839-8503

Per Fotland − *Equinor ASA, 5020 Bergen, Norway*

Geir Ersland − *Department of Physics and Technology, University of Bergen, 5020 Bergen, Norway*

Complete contact information is available at: https://pubs.acs.org/10.1021/acs.energyfuels.1c00549

Notes

The authors declare no competing financial interest.

ACKNOWLEDGMENTS

This work was supported by funding from the Norwegian Research Council. Equinor ASA is thanked for permission to publish this work.

REFERENCES

(1) Boswell, R.; Schoderbek, D.; Collett, T. S.; Ohtsuki, S.; White, M.; Anderson, B. J. The Iġnik Sikumi Field Experiment, Alaska North Slope: Design, Operations, and Implications for CO2−CH4 Exchange in Gas Hydrate Reservoirs. *Energy Fuels* **2017**, *31*, 140−153.

(2) Konno, Y.; Fujii, T.; Sato, A.; Akamine, K.; Naiki, M.; Masuda, Y.; Yamamoto, K.; Nagao, J. Key Findings of the World's First Offshore Methane Hydrate Production Test off the Coast of Japan: Toward Future Commercial Production. *Energy Fuels* **2017**, *31*, 2607−2616.

(3) Yamamoto, K.; Dallimore, S. Aurora-JOGMEC-NRCan Mallik 2006−2008 gas hydrate research project progress. *Fire in the Ice* **2008**, No. Summer, 1−8.

(4) Moridis, G. J.; Kowalsky, M. B.; Pruess, K. Depressurization-Induced Gas Production From Class-1 Hydrate Deposits. *SPE Reservoir Eval. Eng.* **2007**, *10*, 458−481.

(5) Boswell, R.; Collett, T. S. Current perspectives on gas hydrate resources. *Energy Environ. Sci.* **2011**, *4*, 1206−1215.

(6) Yoneda, J.; Masui, A.; Konno, Y.; Jin, Y.; Kida, M.; Katagiri, J.; Nagao, J.; Tenma, N. Pressure-core-based reservoir characterization for geomechanics: Insights from gas hydrate drilling during 2012−2013 at the eastern Nankai Trough. *Mar. Pet. Geol.* **2017**, *86*, 1−16.

(7) Kwon, T.-H.; Oh, T.-M.; Choo, Y. W.; Lee, C.; Lee, K.-R.; Cho, G.-C. Geomechanical and Thermal Responses of Hydrate-Bearing Sediments Subjected to Thermal Stimulation: Physical Modeling Using a Geotechnical Centrifuge. *Energy Fuels* **2013**, *27*, 4507−4522.

(8) Uchida, S.; Klar, A.; Yamamoto, K. Sand production model in gas hydrate-bearing sediments. *International Journal of Rock Mechanics and Mining Sciences* **2016**, *86*, 303−316.

(9) Wu, N.; Li, Y.; Chen, Q.; Liu, C.; Jin, Y.; Tan, M.; Dong, L.; Hu, G. Sand Production Management during Marine Natural Gas Hydrate Exploitation: Review and an Innovative Solution. *Energy Fuels* **2021**, *35*, 4617−4632.

(10) Han, G.; Kwon, T.; Lee, J. Y.; Kneafsey, T. J. Depressurization-Induced Fines Migration in Sediments Containing Methane Hydrate: X-Ray Computed Tomography Imaging Experiments. *J. Geophys. Res.: Solid Earth* **2018**, *123*, 2539−2558.

(11) Waite, W. F.; Jang, J.; Collett, T. S.; Kumar, P. Downhole physical property-based description of a gas hydrate petroleum system in NGHP-02 Area C: A channel, levee, fan complex in the Krishna-Godavari Basin offshore eastern India. *Mar. Pet. Geol.* **2019**, *108*, 272−295.

(12) Torres, M. E.; Tréhu, A. M.; Cespedes, N.; Kastner, M.; Wortmann, U. G.; Kim, J. H.; Long, P.; Malinverno, A.; Pohlman, J. W.; Riedel, M.; Collett, T. Methane hydrate formation in turbidite sediments of northern Cascadia, IODP Expedition 311. *Earth Planet. Sci. Lett.* **2008**, *271*, 170−180.

(13) Santamarina, J. C.; Dai, S.; Terzariol, M.; Jang, J.; Waite, W. F.; Winters, W. J.; Nagao, J.; Yoneda, J.; Konno, Y.; Fujii, T.; Suzuki, K. Hydro-bio-geomechanical properties of hydrate-bearing sediments from Nankai Trough. *Mar. Pet. Geol.* **2015**, *66*, 434−450.

(14) Uchida, T.; Takeya, S.; Chuvilin, E. M.; Ohmura, R.; Nagao, J.; Yakushev, V. S.; Istomin, V. A.; Minagawa, H.; Ebinuma, T.; Narita, H. Decomposition of methane hydrates in sand, sandstone, clays, and glass beads. *J. Geophys. Res.* **2004**, *109*, B05206.

(15) Kumar Saw, V.; Udayabhanu, G.; Mandal, A.; Laik, S. Methane Hydrate Formation and Dissociation in the Presence of Silica Sand and Bentonite Clay. *Oil Gas Sci. Technol.* **2015**, *70*, 1087−1099.

(16) White, M. D.; et al. An international code comparison study on coupled thermal, hydrologic and geomechanical processes of natural gas hydrate-bearing sediments. *Mar. Pet. Geol.* **2020**, *120*, 104566.

(17) Wilder, J. W.; Moridis, G. J.; Wilson, S. J.; Kurihara, M.; White, M. D.; Masuda, Y.; Anderson, B. J.; Collett, T. S.; Hunter, R. B.; Narita, H. An international effort to compare gas hydrate reservoir simulators. *Proceedings of 6th International Conference on Gas Hydrates (ICGH 2008), Vancouver, Canada*; National Energy Technology Laboratory: 2008.

(18) Liu, Y.; Gamwo, I. K. Comparison between equilibrium and kinetic models for methane hydrate dissociation. *Chem. Eng. Sci.* **2012**, *69*, 193−200.

(19) Yin, Z.; Khurana, M.; Tan, H. K.; Linga, P. A review of gas hydrate growth kinetic models. *Chem. Eng. J.* **2018**, *342*, 9−29.

(20) Uddin, M.; Coombe, D.; Law, D.; Gunter, B. Numerical Studies of Gas Hydrate Formation and Decomposition in a Geological Reservoir. *J. Energy Resour. Technol.* **2008**, *130*, 032501.

(21) Moridis, G.; Pruess, K. *User's Manual of the TOUGH+ v1. 5 Core Code: A General Purpose Simulator of Non-isothermal Flow and Transport through Porous and Fractured Media*; Report LBNL-6871E; Lawrence Berkeley National Laboratory: Berkeley, CA, 2014.

(22) Palodkar, A. V.; Jana, A. K. Gas hydrate dynamics in distributed porous particles with saltwater: Model formulation and experimental validation. *Chem. Eng. J.* **2020**, *392*, 123660.
(23) Sun, X.; Mohanty, K. K. Kinetic simulation of methane hydrate formation and dissociation in porous media. *Chem. Eng. Sci.* **2006**, *61*, 3476−3495.
(24) Moridis, G. *User's Manual for the HYDRATE v1. 5 Option of TOUGH+ v1. 5: A Code for the Simulation of System Behavior in Hydrate-Bearing Geologic Media*; Report LBNL-6869E; Lawrence Berkeley National Laboratory: Berkeley, CA, 2014.
(25) Gamwo, I. K.; Liu, Y. Mathematical Modeling and Numerical Simulation of Methane Production in a Hydrate Reservoir. *Ind. Eng. Chem. Res.* **2010**, *49*, 5231−5245.
(26) Moridis, G. J.; Collett, T. S.; Dallimore, S. R.; Satoh, T.; Hancock, S.; Weatherill, B. Numerical studies of gas production from several CH4 hydrate zones at the Mallik site, Mackenzie Delta, Canada. *J. Pet. Sci. Eng.* **2004**, *43*, 219−238.
(27) Li, B.; Li, X.-S.; Li, G.; Chen, Z.-Y. Evaluation of gas production from Qilian Mountain permafrost hydrate deposits in two-spot horizontal well system. *Cold Reg. Sci. Technol.* **2015**, *109*, 87−98.
(28) Sun, J.; Ning, F.; Zhang, L.; Liu, T.; Peng, L.; Liu, Z.; Li, C.; Jiang, G. Numerical simulation on gas production from hydrate reservoir at the 1st offshore test site in the eastern Nankai Trough. *J. Nat. Gas Sci. Eng.* **2016**, *30*, 64−76.
(29) Jin, G.; Lei, H.; Xu, T.; Xin, X.; Yuan, Y.; Xia, Y.; Juo, J. Simulated geomechanical responses to marine methane hydrate recovery using horizontal wells in the Shenhu area, South China Sea. *Mar. Pet. Geol.* **2018**, *92*, 424−436.
(30) Li, B.; Li, X.-S.; Li, G. Kinetic studies of methane hydrate formation in porous media based on experiments in a pilot-scale hydrate simulator and a new model. *Chem. Eng. Sci.* **2014**, *105*, 220−230.
(31) Yin, Z.; Moridis, G.; Tan, H. K.; Linga, P. Numerical analysis of experimental studies of methane hydrate formation in a sandy porous medium. *Appl. Energy* **2018**, *220*, 681−704.
(32) Kowalsky, M. B.; Moridis, G. J. Comparison of kinetic and equilibrium reaction models in simulating gas hydrate behavior in porous media. *Energy Convers. Manage.* **2007**, *48*, 1850−1863.
(33) Kim, H. C.; Bishnoi, P. R.; Heidemann, R. A.; Rizvi, S. S. H. Kinetics of methane hydrate decomposition. *Chem. Eng. Sci.* **1987**, *42*, 1645−1653.
(34) Almenningen, S.; Graue, A.; Ersland, G. Experimental Investigation of Critical Parameters Controlling CH4-CO2 Exchange in Sedimentary CH4 Hydrates. *Energy Fuels* **2021**, *35*, 2468−2477.
(35) Almenningen, S.; Fotland, P.; Ersland, G. Magnetic Resonance Imaging of Methane Hydrate Formation and Dissociation in Sandstone with Dual Water Saturation. *Energies* **2019**, *12*, 3231.
(36) Birkedal, K. A.; Freeman, C. M.; Moridis, G. J.; Graue, A. Numerical Predictions of Experimentally Observed Methane Hydrate Dissociation and Reformation in Sandstone. *Energy Fuels* **2014**, *28*, 5573−5586.
(37) Clarke, M.; Bishnoi, P. R. Determination of the activation energy and intrinsic rate constant of methane gas hydrate decomposition. *Can. J. Chem. Eng.* **2001**, *79*, 143−147.
(38) Stone, H. Probability model for estimating three-phase relative permeability. *JPT, J. Pet. Technol.* **1970**, *22*, 214−218.
(39) van Genuchten, M. T. A Closed-form Equation for Predicting the Hydraulic Conductivity of Unsaturated Soils. *Soil Science Society of America Journal* **1980**, *44*, 892−898.
(40) Bagherzadeh, S. A.; Moudrakovski, I. L.; Ripmeester, J. A.; Englezos, P. Magnetic Resonance Imaging of Gas Hydrate Formation in a Bed of Silica Sand Particles. *Energy Fuels* **2011**, *25*, 3083−3092.
(41) Seol, Y.; Kneafsey, T. J. X-ray computed-tomography observations of water flow through anisotropic methane hydrate-bearing sand. *J. Pet. Sci. Eng.* **2009**, *66*, 121−132.
(42) Priegnitz, M.; Thaler, J.; Spangenberg, E.; Schicks, J. M.; Schrötter, J.; Abendroth, S. Characterizing electrical properties and permeability changes of hydrate bearing sediments using ERT data. *Geophys. J. Int.* **2015**, *202*, 1599−1612.
(43) Yang, L.; Ai, L.; Xue, K.; Ling, Z.; Li, Y. Analyzing the effects of inhomogeneity on the permeability of porous media containing methane hydrates through pore network models combined with CT observation. *Energy* **2018**, *163*, 27−37.
(44) Sun, J.; Dong, H.; Arif, M.; Yu, L.; Zhang, Y.; Golsanami, N.; Yan, W. Influence of pore structural properties on gas hydrate saturation and permeability: A coupled pore-scale modelling and X-ray computed tomography method. *J. Nat. Gas Sci. Eng.* **2021**, *88*, 103805.
(45) Almenningen, S.; Iden, E.; Fernø, M. A.; Ersland, G. Salinity Effects on Pore-Scale Methane Gas Hydrate Dissociation. *Journal of Geophysical Research: Solid Earth* **2018**, *123*, 5599−5608.

https://doi.org/10.1021/acs.energyfuels.1c00549
Energy Fuels 2021, 35, 9836−9846